Numerical optimization of microfluidic vortex shedding for genome editing human primary T cells using machine learning

Justin A. Jarrell[1], Adrian A. Lievano[1], Fong L. Pan[1], Katherine H.W.J. Lau[1], Giles T. S. Kirby[2] and Ryan S. Pawell[1]

1. Indee Labs, Berkeley, CA, United States

2. Future Industries Institute, University of South Australia, Mawson Lakes, SA, Australia

Abstract

Microfluidic vortex shedding (*μVS*) can rapidly deliver mRNA to human T cells with high yield and minimal perturbation. However, the mechanistic underpinning of *μVS* as an intracellular delivery method remains undefined with no optimization framework. Herein, we evaluated a series of *μVS* devices containing various splitter plates to attenuate vortex shedding and understand the contribution of force and frequency on expression efficiency and cell viability. We selected and applied a *μVS* design to knockout the expression of the endogenous T cell receptor of T cells via delivery of Cas9-RNP. 255 *μVS* samples were characterized across more than 150 parameters and machine learning was used to identify the 11 most predictive parameters for expression efficiency and cell viability. These results demonstrate the utility of *μVS* for genome editing of human T cells with CRISPR-Cas9 and provide a robust framework to optimize *μVS* for various constructs, cell types and protocols.

Introduction

Intracellular delivery is a critical process in medicine and biology where exogenous materials are delivered across the cell membrane and into the cytosol. The intracellular delivery of various constructs (i.e. DNA, RNA, protein and complexes) into cells allows for fundamental and exploratory research in cellular and molecular biology and synthesis of engineered cells as therapies[1]. The development of a high-throughput, easy-to-use, and scalable microfluidic technology for intracellular delivery has the potential to dramatically and rapidly improve the discovery process in research while also promising to accelerate the clinical development and commercial manufacture of life-extending T cell immunotherapies like chimeric antigen receptor T cells (CAR-T)[2] and T cell Receptor T cells (TCR-T)[3].

μVS represents a simple and scalable approach to intracellular delivery[4]. Based on the fluid dynamics phenomena of vortex shedding, *μVS* is induced upon fluid flowing past a bluff body (i.e., a micron-scale post in a microfluidic device) creating alternating low-pressure regions downstream of the bluff body. The hydrodynamic conditions created by *μVS* are capable of permeabilizing the lipid bilayer of the cellular membrane to induce transient poration and permit intracellular delivery[4]. However, despite these promising characteristics and potential, the fundamental physics contributing to *μVS* remains unclear. Thus, the development of *μVS* as an effective platform for cellular modification requires an improved understanding of vortex shedding to apply *μVS* in the intracellular delivery of additional constructs, cell types and conditions.

To this end, we develop a series of three-dimensional, transient, single-phase computational fluid dynamics models of *μVS*. We generated *μVS* designs that attenuate vortices through the addition of a 'splitter plate' between post columns of a six column post array[5]. Using our fluid dynamics model, we demonstrated that reductions in splitter plate lengths enhanced vortex shedding and correlated

with increased delivery efficiency. These effects were subsequently validated through fabrication of splitter plate devices and delivery of eGFP mRNA to activated primary human T cells via *μVS*. To explore its potential broader applications, we then applied *μVS* to the delivery of Cas9 and gRNA targeting the T cell receptor alpha locus (TRAC-1), as a Cas9-RNP complex and successfully knocked out the expression of the endogenous T cell receptor of primary human T cells.

To better understand how various conditions, including experimental parameters, device designs and materials, contribute to *μVS* intracellular delivery, we created a database comprised of 255 *μVS*-modified cell samples with greater than 150 parameters and applied Gradient Boosted Decision Tree[6] machine learning modeling to identify parameters that were highly predictive of delivery efficiency and viability. Our analysis of this dataset revealed important predictive parameters of intracellular delivery for various constructs (i.e. DNA, RNA and protein) to support the development of future applications of *μVS*.

Results

Hydrodynamic simulations demonstrate reductions in vortex shedding with inclusion of splitter plates. A series of splitter plates were incorporated into a previously reported *μVS* device design[4] to evaluate the mechanistic underpinning of microfluidic vortex shedding. Empirical measurements of the inlet and outlet pressures and single-phase fluid properties indicated an object Reynolds number of 127 similar to previous reports[5] that was used for simulations. Splitter ratio was defined as the ratio between the length of the splitter plate (a thin object between two consecutive columns of posts) and the center-to-center distance of two consecutive cylindrical posts in the flow-wise direction. Separation ratio was defined as the ratio of the distance between the center of the cylindrical post (in the 2D-plane, this is the circle of the circle) and the leading edge of the splitter plate to the diameter of the cylindrical post. Together, these ratios resolved five device designs, each with a unique splitter ratio: 0, 0.25, 0.50, 0.75, and 1.0 (Figure 1). The separation ratios for these devices are found in Table 1.

The Computational Fluid Dynamics (CFD) simulation results provided detailed primary flow data including hydrodynamics pressure, flow velocity and microfluidic vorticity used to evaluate flow dynamics. In particular, these flow parameters were selected to investigate vortex structures and shedding behavior in the computational domain. In this study, vortex shedding fluctuations were measured quantitatively based on hydrodynamics fluctuating forces acting on cylindrical posts. Vortex structure scales were visualized qualitatively with the aid of spanwise vorticity fluctuation contours and Q-criterion iso-surfaces. To quantify the hydrodynamics performance of each splitter plate device, a performance indicator referred to as the Post Near Wake Indicator (PNWI) was created (see SI - Detailed Simulation Analysis). PNWI values were calculated for each splitter plate device and a ratio was created relative to a baseline configuration (splitter ratio = 1.0) to rank their hydrodynamic performance.

Our simulation results indicated that both spanwise hydrodynamics fluctuating force and PNWI increased with a reduction in splitter ratio (Table 1, Figure 2A, B). In fact, a splitter ratio ≥0.50 showed minimal to no vortex shedding due to vortex attenuation by inclusion of the splitter plates. The total spanwise hydrodynamics fluctuating forces in 1.0, 0.75, 0.50 splitter ratio devices was determined to be approximately 3.9 μN, 6.4 μN, and 8.7 μN, respectively. The magnitude of these fluctuations were much greater with 0.25 and 0.0 splitter ratio devices at approximately 134 μN and 336 μN, respectively. Similarly, the PNWI values of 0.25 and 0.0 splitter ratio devices were also determined to be greater than devices with splitter plate ratios ≥0.50 at 40% and 100%, respectively (Table 1). These PNWI and fluctuating force numericals highlighted a substantial increase in vortex strength in the simulated devices without splitter plates. The measurements also suggested that when splitter plates were placed sufficiently close to the base of cylindrical post, the vortex street (i.e. 'swirling vortices') failed to develop. In general, our Design of Experiment (DOE) study here demonstrated an consistent inverse correlation in PNWI and fluctuating force and the splitter plate ratio.

In addition, the simulation results also provided evidence of vortex structures present in the device as quantified by the vortex shedding frequency. Vortex shedding frequency was quantified from the periodic form of oscillation of the vortex structures behind the posts. It was found that only 0.25 and 0.0 splitter ratio devices exhibited consistent periodic oscillation of the dominant vortex shedding, at the rate of 36 kHz and 13.5 kHz, respectively (Table 1, Supplemental Figure 3). Minimal to no vortex shedding was observed in the 0.5, 0.75, or 1.0 splitter configurations with zero frequency detected. Furthermore, vortex shedding spectral analysis also suggested that vortex suppression occured when the separation ratio was less than 3.25 (SIM01-03, splitter ratio 1.0 - 0.5) , similar to previous reports[5]. Numerical analysis also revealed that vortex formation inside the wake region occurred as

a result of two ('pair') of counter-rotating vortices developed behind a post (Supplemental Figure 4). In the 0.0 splitter ratio device, the wavelength of its vortex pairs was approximately 6 times the post diameter (240μm). This is consistent with the computed vortex convection speed of 3 m s^{-1} at frequency rate of 13.5kHz based on wavelength-frequency relationship. However, in the 0.25 splitter ratio device, the presence of the splitter plate with a separation ratio of 3 interfered with oscillation downstream of the posts while full oscillating wavelengths were undetectable in the 1.0, 0.75, and 0.5 splitter ratio devices (see Supplemental Figure 2B). The device design simulated with a separation ratio of 3 (SIM04, 0.25 splitter ratio) resulted in a higher frequency of vortex oscillation with lower spanwise hydrodynamic forces when compared to SIM05 (0 splitter ratio) (Table 1, Supplemental Figure 3). While the underlying mechanism of higher rate vortex shedding generation is better understood through our simulation of *μVS* devices with inclusion of finite length splitter plates, the impact of the actual vortex oscillation on the delivery efficiency in cells has yet to be fully resolved.

The hydrodynamics pressure distribution contour indicated that the fluid pressure remains uniform in regions between consecutive post columns. Such hydrodynamics pressure distribution was unperturbed in the presence of vortex shedding structures in 0.0 and 0.5 splitter ratio devices (Supplemental Figure 1). Pressure uniformity was self-sustained by a pair of counter-rotating vortex similar strength oscillating at both symmetrical sides of the post (Supplemental Figure 1 and 2). The pressure distribution remaining undisturbed in the presence of vortex shedding inferred that the flow dynamics in the chip would remain unchanged. Therefore, it is speculated that the flow rates for all splitter ratio devices remained consistent at a given applied pressure.

Vortex structure behavior was also detected by measurement of Q-criterion iso-surfaces (Supplemental Figure 4). Q-criterion analysis indicated that the vortex structures were oscillating at

higher amplitude in the downstream columns (4-6) compared to upstream columns (1-3) of the 0.0 and 0.25 splitter ratio devices. Based on this, it is speculated that the number of post columns included in a device design will impact the overall device performance (delivery efficiency) due to vortex amplitude enhancement. The self-sustained vortex fluctuations behavior in the downstream columns are thought to further enhance device performance as an intracellular delivery method.

Vortex shedding correlates with delivery efficiency and cell viability Fluid dynamic modeling highlighted correlations between vortex shedding and delivery efficiencies. We evaluated these results empirically by fabricating splitter plate devices for intracellular delivery to activated CD3+ T cells with mRNA and quantify eGFP expression and cell viability after delivery via *μVS*. Similar to our simulations, we observed an incremental decrease in eGFP expression 24 hours after *μVS* correlated with an increase in splitter plate lengths, ranging from 51.8% to 11.8% eGFP expression between 0 and 1.0 ratio splitter plate devices, respectively, (Figure 3A, Table 2). Conversely, we observed an increase in cell viability with the attenuation of vortex shedding. However, unlike eGFP expression, the elevated levels in cell viability were non-incremental, with the largest difference occurring between 0.5 and 0.75 splitter plates with 44.6 and 66.9% live cells quantified, respectively (Figure 3B, Table 2). In comparison to numerical predicted vortex shedding, our experimental results validate a continuous decrease and inverse correlation with delivery efficiency, with a non-incremental, positive correlation with cell viability.

Cas9-mediated genome editing achieved with *μVS* To address the potential broad application of *μVS* beyond intracellular delivery of mRNA, we evaluated the utility of *μVS* for CRISPR-Cas9-based T cell engineering. Using *μVS*, we delivered Cas9 and gRNAs (as a Cas9-RNP complex) targeting the first exon of the TCR-alpha constant region (TRAC-1) in primary human activated CD3+ T cells. As a proxy for delivery efficiency, we evaluated TCRa/b and CD3

co-expression in the *μVS*-modified cell population. We quantified co-expression at 4 days after intracellular delivery and observed a significant decrease in TCR/CD3 expression, with an editing efficiency of 37.4% of live cells relative to cells modified with an off-target gRNA and non-*μVS* controls (Figure 4A) . Sustained reductions in TCR/CD3 expression were also observed at days 7 and 14 post-*μVS* with editing efficiencies of 36.9% and 36%, respectively, indicating locus-specific deletion of TCR-a and persistent genome modification with Cas9-RNP and *μVS* (Figure 4B). Cell viability remained high at and after 4 days post-*μVS* (>80% at days 4 and 7, >70% at day 14, Figure 4C).

To assess T cell expansion, we quantified the number of TCR/CD3 knockout cells achieved for the duration of the experiment. Cas9-RNP knockout via *μVS* resulted in 4.4 x 10^7 cells $flask^{-1}$ (~120mL) of genetically-modified, viable knockout cells on day 14 post-*μVS* (Figure 4D). We observed incremental increases in the fold change of TCR/CD3 knockout cells achieved in TRAC-1-targeting Cas9-RNP compared to controls, with an 89-fold increase at 14 days post-*μVS*, providing evidence of sustained, modified T cell expansion (Figure 4E). Collectively, these results demonstrate the successful delivery of Cas9-RNPs to T cells via *μVS* for rapid *in vitro* gene editing with the potential to scale to processing capacities required for clinical applications.

Machine learning model predicts delivery efficiency with *μVS* After a series of data preprocessing and exploration steps (outlined in the methods section), we narrowed the total number of features used to build our intracellular delivery prediction model by first measuring the degree of multicollinearity in the input data. Correlated data columns (i.e. evaluated using a R2-score coefficient) that are used to train the machine learning model were removed from the data. This is a standard preprocessing step in machine learning model optimization[7].

A machine learning model, known as Gradient Boosted Decision Trees[6], was trained across simulation and experiment data and achieved a R-squared value of 0.569 (Figure 5A, B). The algorithm identified the 11-most important parameters contributing to this score (>2% percent prediction importance) that included biological (cell type, delivery material), numerical (average post-gap pressure differential, dominant vortex shedding frequency), and process-driven (input pressure, number of cell activations) (Figure 5C). This specific model was selected after using grid-search hyperparameter optimization techniques and iterating over 20 different regression-based machine learning models. A gradient boosted tree using the input parameter to predict 24-hour delivery efficiency was also created. (Figure 5D). Our trained model produced an error distribution with a mean value of -0.415. The error was calculated by using the difference between the predicted and actual delivery efficiencies. The standard deviation of our error distribution was 9.926.

Discussion

Splitter plate simulations & experimentation The use of splitter plates of variable finite lengths allowed us to analyze the influence of vortex shedding on delivery efficiency and cell viability in a manner where the influence of pressure changes and vorticity experienced by cells could be reasonably decoupled. Splitter plate designs were able to completely attenuate vortex shedding with a splitter ratio less than 0.5 with only partial levels of vortex shedding occuring in devices with a splitter ratio of 0.25. The highest levels of vortex shedding was observed in our original *μVS* device with no splitter plate. All of this is in agreement with the fundamental splitter plate studies performed by Unal and Rockwell[5] at similar object Reynolds numbers.

Interestingly, a trend between these simulation parameters (spanwise hydrodynamics fluctuations and the PNWI) and the eGFP expression efficiency of mRNA and T cell viability is observed. As the splitter ratio of the *μVS* device decreases, the delivery efficiency increases, which is correlated to the rise of the spanwise hydrodynamics fluctuations and vortex shedding frequency in simulations (Table 2, Figures 2 and 3). Similarly, previous studies have also demonstrated a negative correlation between delivery efficiency and cell viability[4]. In the *μVS* splitter devices, a comparable trend emerged with enhanced delivery efficiency correlating with a reduction in splitter plate lengths and dimensioned cell viability.

Discontinuities were also observed in simulation and empirical results highlighted in our analysis of the *μVS* device with a 0.5 splitter ratio. Despite simulating an absence of vortex shedding and minimal spanwise fluctuating hydrodynamic forces, eGFP expression was observed in the 0.5 splitter ratio devices. We speculated that the delivery of eGFP mRNA in cells could be due to the presence of early-onset, cell-induced vortex shedding that was not captured in our single-phase simulations. Single-phase simulations are limited in their ability to capture nuanced vortex shedding

and will likely require transient, multi-phase approaches to simulate suspensions cells to better understand the contribution of vortex shedding on delivery efficiency. Multi-phase simulations are currently under development.

A key limitation in our current study also includes correlating computational and numerical parameters to empirical results on biological systems (cell age and growth, activation time etc.), which are not directly. Improvements to this framework would include the empirical quantification of transient hydrodynamic forces and vortex shedding frequencies for each *μVS* device design combined with multi-phase simulation studies. Despite these limitations, our study serves as a foundation to use simulations to better understand *μVS* as a new effective method for intracellular delivery.

CRISPR-Cas9 & *μVS* The CRISPR-Cas9 genome editing system has emerged as a promising approach to generate cell-based immunotherapies without the use of viral vectors. Recently, T cells engineered to express an exogenous T cell receptor targeting tumor antigens via delivery of Cas9-RNP and DNA templates have been shown to mount effective anti-tumor responses *in vitro* and in murine models[8], and in early stage clinical trials[3]. To explore the utility of *μVS* as an intracellular delivery method for CRISPR-Cas9 editing, we delivered Cas9 protein complexed to gRNA targeting the T cell receptor alpha locus (TRAC-1) to knock out the expression of the endogenous T cell receptor and permanently modify primary human T cells. We demonstrated >35% editing efficiency in live T cells at 4 days post-*μVS*, which is similar to the TRAC-1 editing efficiencies observed in the first-in-human phase I clinical trial with multiplex CRISPR-Cas9 editing[3]. Genome editing persisted for an additional 10 days for the duration of the experiment. Further, cell viabilities were greater than 80% at 4 and 7 days after *μVS*, with levels remaining above 70% at day 14, exceeding the product release criteria for clinical use of current CAR-T cell therapies[2].

Accompanying delivery efficiency and viability as important factors to generate effective cell therapies, the ability to synthesize a sufficient number of modified cells to dose patients is a critical factor in successful treatment in the appropriate time frame[2,3]. In our studies, we were able to generate >4.0 x 10^7 viable genetically-modified, TCR/CD3-negative T cells in ~120mL of culture media at 14 days post-*μVS* when delivering TRAC-1-targeting Cas9-RNP to 3.75 x 10^6 T cells. Based on the growth curve of our study (y = 3.5194x - 5.4404 where x is the day post-*μVS*), and starting with 1.5 x 10^7 T cells for *μVS*, we estimate achievement of 1.2 to 2.5 x 10^8 cells between days 10 and 19 post-*μVS*. Greater quantities of genome edited cells[3] could also be obtained by processing 3.0 x 10^7 cells via *μVS* as this is the maximum number of cells that can be processed with the current chip design. Future work to expand the width and depth of the flow cells to further increase our processing capacities, while maintaining the same 5x10mm device dimension, is currently ongoing.

While foundational and preliminary, these data suggest that the processing capacity of *μVS* can readily meet and potentially exceed the quantity of engineered T cells sufficient for clinical applications, while substantially reducing processing time ex vivo required to manufacture T cell therapies. This is particularly important in light of a recent *in vivo* study demonstrating that a reduction in cell culture time (i.e. 3 days) enhanced anti-leukemic activity in CAR-T cells at a 6-fold lower dose[2]. The rapid gene editing time frames, coupled with the development of *μVS* design with higher cell processing capacity, highlights the potential of *μVS* to substantially reduce clinical and commercial manufacturing time frames. These results establish the early processing capacity of *μVS* and highlight the potential of *μVS* as a platform for intracellular delivery towards the clinical development and commercial production of T cell immunotherapies like CAR-T and TCR-T.

Database and Machine Learning Machine learning models aim to optimize the performance of a certain task. In the case of delivery efficiencies for *μVS*, our database and model optimization demonstrated the ability to predict 24 hour delivery efficiency given an input set of more than 150 unique biological, computational, and process-driven feature parameter.

From initial exploration of these training and testing results of the machine learning model on our dataset, we were able to better understand which feature parameters impacted the delivery efficiency of various constructs (i.e. DNA, mRNA and protein complexes). Interestingly, biological and computational features, including cell culture age (days) and averaged post fluctuating lift force, were among the top 11 parameters used to predict the efficiencies at 24 hours post-*μVS* delivery.

These insights empower researchers with the ability to select a predefined set of prediction features and determine, before operating an experiment, the predicted delivery efficiency at 24 hours. The prediction algorithm considers the type of construct and output values that, over time, if given more training data, are likely to approach experimental averages. These same results and machine learning techniques can be further applied to predict delivery efficiencies up to two weeks from the initial point of *μVS*. As the database continues to expand, and more training examples are included to represent a larger sampling distribution of different cell types and sample constructs, we anticipate an improved prediction performance to optimize and create novel device designs for future applications.

Conclusion

Our investigation of vortex shedding via simulations, experimentation and machine learning, provides a better understanding of the parameters (biological, physical, material etc.) contributing to vortex shedding and *μVS* as a method for intracellular delivery. We demonstrated a novel application of *μVS* for genome editing in activated human T cells with the CRISPR-Cas9 genome-editing system. Further, we presented a data-driven framework identifying key parameters for the optimization and application of *μVS* for other cell types, constructs and conditions.

Studies to deliver Cas9-RNPs with DNA templates and use of a transposon/ase system with *μVS* to engineer cells with knock-in expression are currently ongoing. Future simulation efforts will iterate on various device design parameters, such as post diameter, and will be used to study the effects of fluctuating lift force and PWNI on delivery efficiency. These results will expedite the development of future *μVS* devices optimized to deliver a variety of constructs and cell types. 3D transient, multiphase simulations are being explored on various device designs to expedite development of future *μVS* devices and applications beyond T cells.

Methods

Splitter plate device design & simulation A total of five splitter plate device CAD geometries were designed and constructed using OnShape software. The geometries were computationally meshed and simulated with OpenFOAM software to evaluate and investigate the influence of vortex shedding on cell viability, mRNA delivery and subsequent eGFP expression. Splitter ratios for these devices were 1.0, 0.75, 0.5, 0.25 and 0 while separation ratios were 0, 0.75, 2, 3.25 and 10, respectively.

Our CFD computational domain consisted of structured (hexagonal) mesh with a total of 30 million grid points. Mesh independent studies were performed to ensure the numerical flow results were sufficiently resolved without the influence of mesh resolution. The finest resolutions used in the device geometry, located near the cylindrical posts, were at a 2μm. This resolution was considered sufficiently to resolve flow shear layer with a total of four grid points across the device in the spanwise direction. The coarsest resolutions, located near the inlet and outlet channels of the device, were set at 8 μm. Slip boundary conditions were not used on walls except for the inlet and outlet channels, which had pressures of 134.7 and 14.7 PSIA, respectively, to create a 120 PSIG pressure drop in each device. A single-phase laminar Reynolds number was used with Opti-MEM at 23°C (ρ = 1011.4 kg m^{-3}, μ = 9.586 x 10^{4} kg m^{-1} s^{-1}) as processing fluid. 3D transient simulations were performed with OpenFOAM 5.0's transient PimpleFOAM single phase solver. A total of 3.5 ms flow through time was simulated with a time-step of 1 μs. An initial transient time of 1.5ms was necessary to allow flow to become fully developed with the numerical schemes. Therefore, a total of 2.0ms of statistical numerical data was collected to resolve flow structures behaviours with a flow spectral frequency from 5kHz to 500KHz. Numerical solutions required 19,800 to 22,800 cpu-hours over 4 days with 198 parallel cores on Rescale and Amazon Web Services supercomputers. Rescale's C4 Instant cluster type was used with Intel Xeon 2.9Hz CPUs with 3.8 GB of memory per core.

***μVS* device fabrication** Devices were fabricated using previously reported, industry standard semiconductor techniques[4]. Briefly, *μVS* device and device features (posts, channel thickness, inlet and outlet channels) were manufactured by (1) generated a digital rendering of the microfluidic using Onshape CAD software, (2) preparing a wafer substrate and (3) performing a series of metallisation, inspection, photolithography, liftoff, and laser drilling on the substrate (Australian National Fabrication Facility, South Australia).

***μVS*-based delivery of eGFP mRNA with splitter plate devices** Primary human CD3+ T cells were isolated from donor PBMCs via immunomagnetic negative selection (Stem Cell Tech). For thaw and culture, cryopreserved T cells were expanded using anti-CD3/CD28 dynabead T cell activator (ThermoFisher) with standard conditions for 2 days, followed by debeading and *μVS*.

All solutions processed through the device and device were filtered prior to use with a 0.22 μm filter to remove particulates. For device processing, T cells were debeaded, washed, resuspended in Opti-Mem (ThermoFisher) and filtered with a sterile 40 μm cell strainer. eGFP-encoding mRNA (TriLink) was delivered at 200 μg mL^{-1} (50 μg mRNA) into activated T cells at 1.5 x 10^7 cells mL^{-1} (3.75 x 10^6 cells) in a total volume of 250 μL with a driving pressure of 120 PSIA. Sample rig and tubing were sterilized before use via 70% ethanol wipe down and flush. Immediately prior to *μVS*, samples were mixed thoroughly by gentle pipetting, mounted in the sample reservoirs and driven pneumatically though the device for intracellular delivery by *μVS*. Processed samples were collected warmed (37°C) media (XVIV020 + 5% human serum, Lonza), and cultured at 1.0 x 10^6 cells mL^{-1} supplemented with IL-2 at 100IU mL^{-1} (Peprotech). Each splitter plate condition was evaluated in

triplicate. eGFP and cell viability levels were quantified by propidium iodide viability staining (ThermoFisher) and flow cytometry (Attune, ThermoFisher Scientific) at 24 hours post-*μVS*.

Genome editing with Cas9-RNP complexes and *μVS* Cas9-RNPs (1:1 Cas9:gRNA molar ratio) were delivered 2 days after initial T cell stimulation. Anti-CD3/-CD28 dynabeads (ThermoFisher) were removed by placing cells on a cell separation magnet for 2-5 mins. Immediately before *μVS*, de-beaded cells were centrifuged for 10 min at 1500rpm, aspirated, resuspended Opti-Mem and filtered with 40μm cell strainer. Cas9-RNPs were delivered at 3.0 x 10^{-5} pmols RNP $cell^{-1}$ to activated T cells at 2.5 x 10^{7} cells mL^{-1} (3.75 x 10^{6} cells $sample^{-1}$) in a total volume of 150uL (10uL RNPs, 140uL cell suspension), with an applied driving pressure of 120 PSIA. Processed samples were collected in warmed (37°C) media (XVIV020 + 5% human serum, Lonza), and cultured at 1.0 x 10^{6} cells mL^{-1} supplemented with IL-2 at 100IU mL^{-1} (Peprotech). IL-2 at 100IU mL^{-1} was supplemented every 2 ~ 3 days post-*μVS*. Each condition was evaluated in triplicate. Levels of TCR and CD3 expression and cell viability and cell expansion were quantified by live/dead staining and the following antibodies via flow cytometry: anti-TCRa/b-PE (306708, BioLegend), anti-CD3-AF700 (11-0039-42, ThermoFisher), Sytox Blue Viability Stain (S34857, ThermoFisher). Flow cytometry analysis was performed on days 1, 4, 7 and 14 post-*μVS*.

Flow cytometry. Flow cytometric analysis was performed on an Attune NxT Acoustic Focusing Cytometer (ThermoFisher). Surface staining for flow cytometry was performed by pelleting cells and resuspending in flow buffer (1% human serum in PBS) with antibodies for 30 min at 4°C in the dark. Cells were washed once in flow buffer prior to resuspension.

Database and machine learning. The database architecture contained 35 biological, 92 hydrodynamic, and >50 process or manufacturing predictor parameters for 255 samples. Custom

data processing pipelines, following industry standard practices of standardization of continuous values and one-hot-encoding of categorical parameters ensured effective predictor model training and evaluation of collinearity effects[7]. Multicollinearity effects were evaluated and highly correlated feature parameters (correlation score above 0.80) were discarded to optimize model performance[7]. Empirical data from each *μVS* experiment performed in-house, including cell type, cell activation technique, buffer media, and cell processing concentrations, were collected by researchers and entered into a data repository and used for modeling. In the hydrodynamic data schema, simulation parameters such as predicted vortex-shedding frequency, vortex-shedding forces (along the flow-wise direction of the device), were tracked. Our process and manufacturing data schema included features that describe the design of a given *μVS* device (number of posts, number of columns, gap space between posts, etc.) and information about any instruments or processing pressures used in the experiment. To analyze this database, we leveraged standard open source python libraries (scikit-learn, pandas, numpy, etc.) and tools such as Jupyter notebooks and DataIku. Extract, transform, and load (ETL) data pipelines were built in dataiku. ETL pipelines consist of cleaning text, numerical, and categorical data. For a column with text data, ETL pipelines lowercase all characters, and removes strings and spaces to ensure columns are easily usable for analysis. ETL pipelines for numeric data standardize the raw data, meaning that values are set to have a mean of zero and a standard deviation of one. This reduces model bias due to scalar differences between predictor parameters. ETL pipelines for categorical data one-hot encode values, meaning that new columns are built to represent the unique categories in a column by a vector of zeros and ones. Standard python libraries, such as pandas and numpy, are used to create and manipulate dataframes. Dataiku is also used to train and test all of our machine learning models.

Acknowledgements

This work was funded in part by IndieBio (indiebio.co), SOSV (sosv.com), Jobs for NSW (jobsfornsw.com.au), Y Combinator (ycombinator.com), AusIndustry (business.gov.au), Social Capital (socialcapital.com), Main Sequence Ventures (mseq.vc), Founders Fund's FF Science (foundersfund.com), Axial (axialsprawl.com), MTP Connect Biomedtech Horizons 1.0 (mtpconnect.org.au/biomedtechhorizons), NSW Health Medical Device Fund (medicalresearch.nsw.gov.au/medical-devices-fund) and an array of angel investors.

The authors are thankful for the simulation and computational support provided by Rescale, Amazon Web Services (AWS) and the OpenFOAM community. This work was performed in part at the South Australia node of the Australian National Fabrication Facility, a company established under the National Collaborative Research Infrastructure Strategy to provide nano- and micro-fabrication facilities for Australia's researchers. The authors would also like to acknowledge Hamish Hawthorn, Ben Wright, David Gottlieb, Kenneth Micklethwaite, Geoff Facer and Heidi Hagen for their guidance, advice and support when pursuing science in the startup environment.

The content is solely the responsibility of the authors and does not necessarily represent the views of anyone acknowledged in this section.

Author Contributions

Conception, experimental design, simulations, analysis and interpretation were performed by J.A.J., A.A.L., F.L.P., K.H.W.J.L., G.T.S.K. and R.S.P. The manuscript was drafted by J.A.J., A.A.L., R.S.P. and F.L.P. Experiments were performed by J.A.J, A.A.L., K.H.W.J.L, and G.T.S.K.

Competing Interests

All authors are consultants, employees, shareholders and/or optionees of Indee. Inc. or the wholly-owned Australian subsidiary Indee. Pty. Ltd. Both legal entities have an interest in commercializing *μVS* and related technologies.

Tables

Table 1 Summary of splitter plate device designs and simulations

Device Designs			**Simulations**		
Design	Splitter Ratio	Separation Ratio	*μVS* Frequency (*Hz*)	Total Spanwise Fluctuating Hydrodynamics Forces on Post (N)	Post-Near Wake Indicator (PNWI)
SIM01	1.0	0	--	3.9E-6	1%
SIM02	0.75	0.75	--	6.4E-06	2%
SIM03	0.50	2	--	8.7E-06	3%
SIM04	0.25	3.25	36,000	1.3E-04	40%
SIM05	0	10	13,500	3.4E-04	100%

Table 2 eGFP expression and cell viability at 24 hours post-*μVS* with splitter plate devices

Device Designs			**Expression & Viability**	
Design	Splitter Ratio	Separation Ratio	Efficiency (%)	Viability (%)
SIM01	1.0	0	11.8 ± 1.55	68.2 ± 5.19
SIM02	0.75	0.75	20.6 ± 0.68	66.9 ± 3.85
SIM03	0.50	2	36.1 ± 0.50	44.6 ± 4.44
SIM04	0.25	3.25	41.6 ± 0.53	41.3 ± 1.62
SIM05	0	10	51.9 ± 2.21	40.8 ± 3.63

Figures

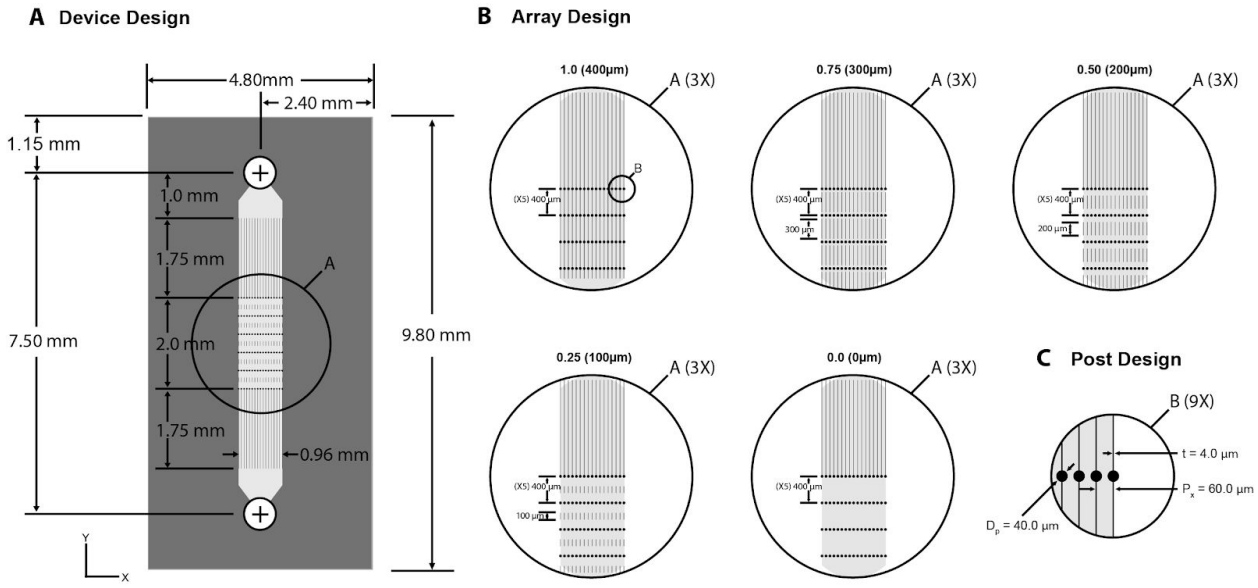

Figure 1. *µVS* device, array and post designs. (A) *µVS* chips fabricated as a 4.80 mm by 9.80mm device with a 7.50mm length and 40µm depth flow cell. Flow cells contained inlet and outlet channels flanking 6 columns of posts of 17 posts per column representing the post array region. (B) Array designs for five *µVS* devices with varied lengths splitter plates (400 - 100µm) or no splitter plates (0.0, 0µm). (C) All posts were identical with 40µm diameter and depth. Splitter plate walls were of 4µm width creating 60µm wide channels.

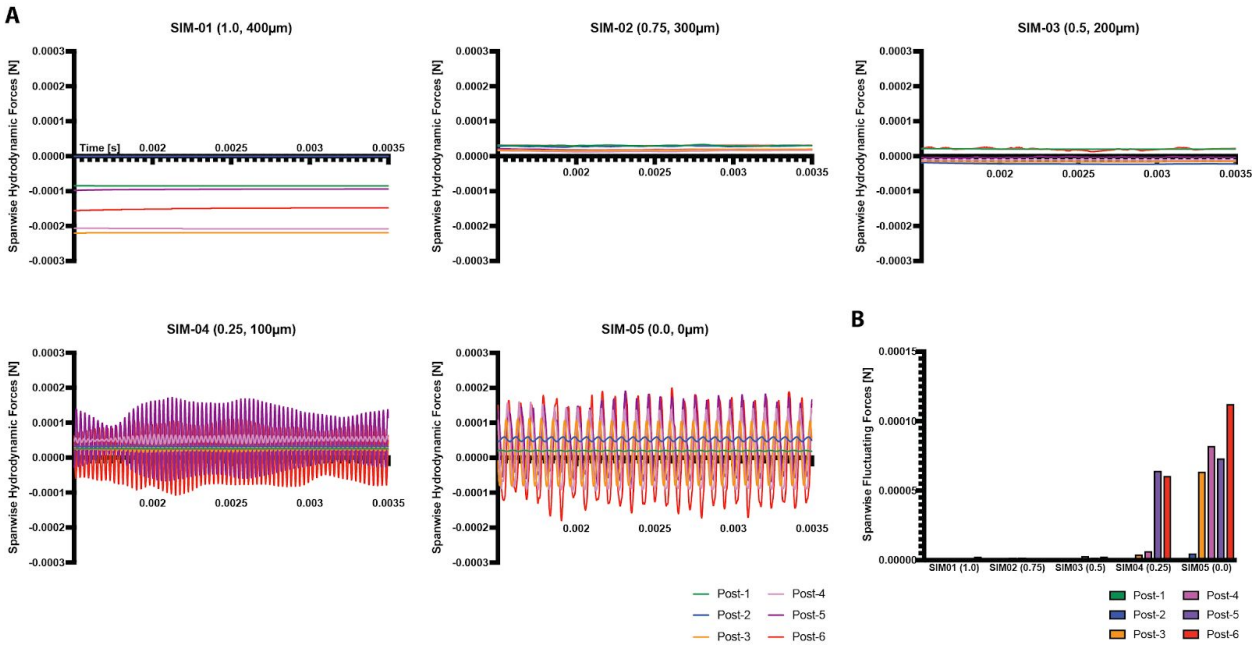

Figure 2. Transient force analysis of *µVS* splitter devices. (A) Spanwise Hydrodynamics Forces [N] on each post column of *µVS* devices with 0.0 - 1.0 splitter ratios in the as a function of time. (B) Spanwise Hydrodynamic Fluctuations on each post column (1 - 6) for each splitter device design.

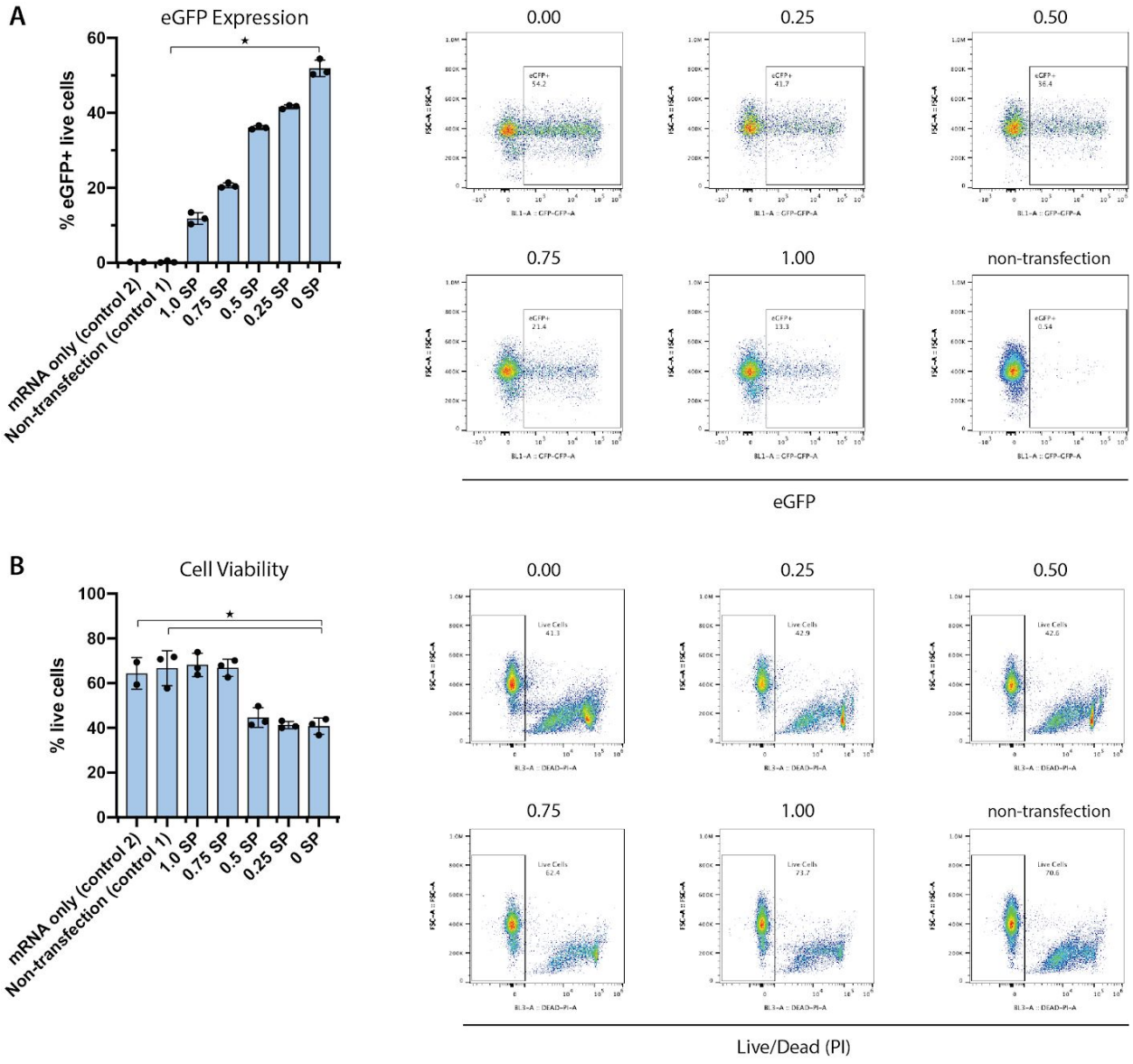

Figure 3. Vortex shedding correlates with delivery efficiency and cell viability when delivering eGFP mRNA to primary activated human T cells via *μVS*. eGFP-encoding mRNA was delivered to activated CD3+ T cells via *μVS* with microfluidic devices containing splitter plates of various lengths. Levels of (A) eGFP expression and (B) cellular viability were quantified at 24 hours post-*μVS*. Data represent the mean ± standard deviation of n = 3 samples per condition. Dot plots representative of triplicate samples with splitter plate ratios and conditions indicated in each plot. *P < 0.05, **P < 0.01, ***P < 0.001 by Kruskal-Wallis.

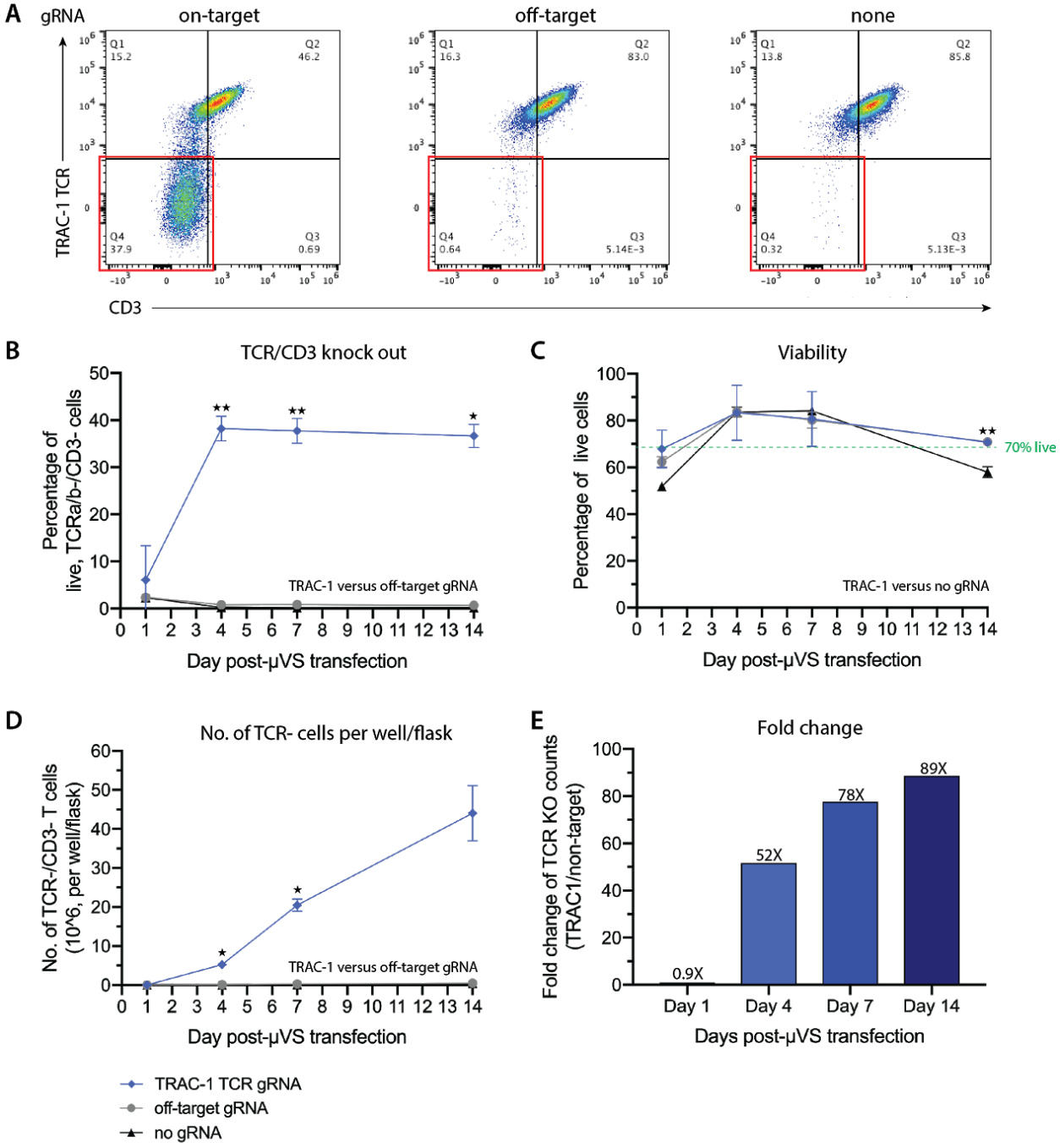

Figure 4. Knockout of endogenous TCR by *μVS*. Cas9 and locus-specific TRAC-1 gRNAs (as Cas9-RNP complexes) were delivered to activated human CD3+ T cells via *μVS*. Off-target gRNA and non-*μVS* samples served as negative controls. (A) Knock out of endogenous TCR expression

with TRAC-1-targeted Cas9-RNP compared to controls. (B) Endogenous TCR expression, (C) cell viability, (D) number of TCR-negative T cells and (E) fold change of TCR KO cell counts between TRAC-1 and off-target controls were quantified on days 1, 4, 7, and 14 post-*μVS*. Data represent the means ± SD of n ≥ 2 samples per condition. Statistical analysis performed between groups indicated on graphs. *P < 0.05, **P < 0.01, ***P < 0.001 by unpaired, two-tailed Student T-test.

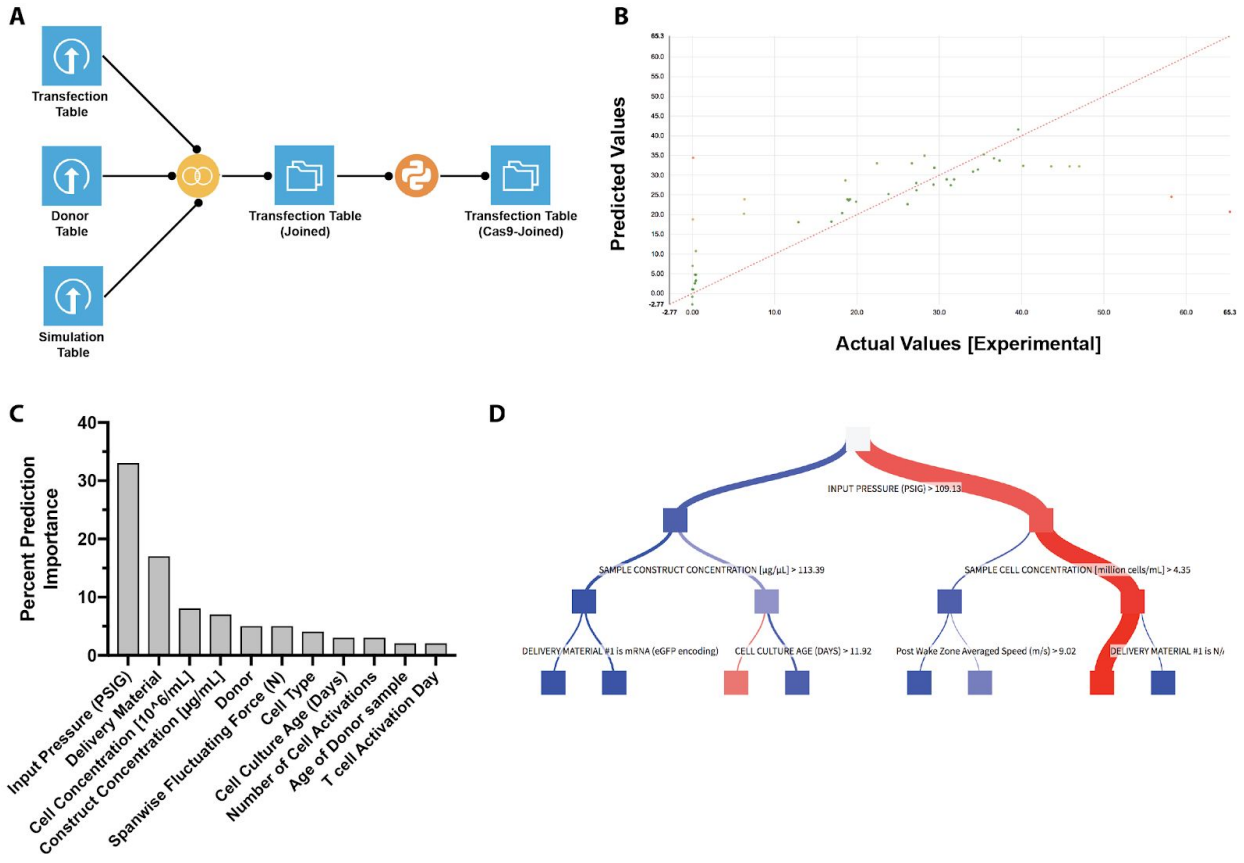

Figure 5. Analyzing Gradient Boosted Decision Performance to Predict *µVS* delivery Efficiency. (A) A data processing and machine learning pipeline architecture designed using Datalku Open Source Software. (B) A linear regression fit model comparing predicted and experimental values at 24 hours after *µVS* delivery. (C) Top 11 ranked predictor parameters (>2% percent prediction importance) of delivery efficacy at 24 hours identified using Gradient Boosted Decision Trees machine learning model. (D) A gradient boosted decision tree using the input parameters to predict 24-hour delivery efficiency.

References

1. Stewart, Martin P., *et al.* "In vitro and ex vivo strategies for intracellular delivery." *Nature* 538.7624 (2016): 183-192.
2. Ghassemi, Saba, *et al.* "Reducing ex vivo culture improves the antileukemic activity of chimeric antigen receptor (CAR) T cells." *Cancer immunology research* 6.9 (2018): 1100-1109.
3. Stadtmauer, Edward A., et al. "CRISPR-engineered T cells in patients with refractory cancer." *Science* (2020).
4. Jarrell, Justin A., *et al.* "Intracellular delivery of mRNA to human primary T cells with microfluidic vortex shedding." *Scientific Reports* 9.1 (2019): 1-11.
5. Unal, M. F., and D. Rockwell. "On vortex formation from a cylinder. Part 2. Control by splitter-plate interference." *Journal of Fluid Mechanics* 190 (1988): 513-529.
6. Ye, Jerry, *et al.* "Stochastic gradient boosted distributed decision trees." *Proceedings of the 18th ACM Conference on Information and Knowledge Management*. 2009.
7. Schmidt, Jonathan, *et al.* "Recent advances and applications of machine learning in solid-state materials science." *NPJ Computational Materials* 5.1 (2019): 1-36.
8. Roth, Theodore L., *et al.* "Reprogramming human T cell function and specificity with non-viral genome targeting." *Nature* 559.7714 (2018): 405-409.

SI - Detailed Simulation Analysis

Centerline Pressure Distribution Supplemental Figure 1 shows the mean-flow hydrodynamics pressure distribution at the centerline of the device. The distribution depicted the pressure variations at the first to last column. The presence of the splitter plates had minimal impact on the hydrodynamics pressure distribution. Local pressure drops were consistently identified across each post column in the streamwise direction for all device designs. Generally speaking, such local pressure drops varied at ~20 psig (1.4 ATM) at by-pass flow duration of 2 μs for all device designs. The local pressure drop was largely dictated by the local flow restriction due to closely aligned posts positioned along each column.

In between columns, the hydrodynamics pressures were uniformly distributed in the spanwise direction. Interestingly, these distributions remained uniform in the absence and presence of vortex shedding. Along the centerline of the chip, local pressure recovery developed in the streamwise direction extending downstream into the far-field region starting from the base of each post. Such pressure recovery development was located at the far-field wake formation as flow convected downstream.

Mean-flow Hydrodynamics Pressure Contour and Instantaneous Spanwise Fluctuating Vorticity Contours Supplemental Figure 1 shows flow-fields colored by absolute pressure and instantaneous spanwise fluctuating vorticity magnitude for all devices. Hydrodynamics pressure in between columns were uniformly distributed in spanwise direction for all configurations in the absence and presence of vortex shedding conditions.

As indicated in Supplemental Figure 1, fluctuating vortices were predominant in both 0.0 and 0.25 splitter ratio devices. Such spanwise fluctuations were considered the footprint of vortex shedding

pairs in their oscillating modes. Red and blue colors in the contours represented counter-rotating vortices pairs with the same strength magnitude. Conversely, hydrodynamics vorticities remain undistorted (remain stationary without oscillation) in the 0.50, 0.75 and 1.0 splitter ratio devices in spanwise direction behind a majority of posts. In particular, more dominant vorticity fluctuations at the last 3 post columns were present in the 0.25 splitter ratio devices whereas uniform fluctuation behaviors across all columns was observed in the 0.5 splitter ratio device.

Therefore, we can conclude that in the presence of the vortex shedding (i.e. 0.25 and 0.0 splitter ratio), the uniform hydrodynamics pressure distribution is undisturbed since the vortex structures are fluctuating in equal and opposite strength and direction at both symmetrical sides of the post. It is expected such a synchronous oscillating pattern of the vortex shedding in both 0.0 and 0.25 splitter cases shall not disrupt the uniformity of the pressure distribution that are similarly found in 0.5-1.0 splitter ratio cases.

Mean-flow Streamwise Velocity Contours Supplemental Figure 2 shows the mean-flow streamwise velocity distributions for all design configurations. The mean-flow streamwise velocity contours provide insight to the extent of wake formation regions in the chip. In the 0% splitter ratio case, the wake regions were widely spreaded in both far and near-field regions indicated by low negative streamwise velocity colored by blue. In contrast, both splitter ratio of 1.0 and 0.75 splitter ratio devices had fewer and narrower wake regions in most fluid domains compared to all other devices. In general, the number of wide wakes found in the domain increased with the reduction in splitter ratio. The presence of a splitter plate at the finite length of 0.50-1.0 splitter ratios showed an attenuation of near-field vortex shedding and therefore prohibited downstream (far-field) wake formation.

The large number of wide wake regions present in the 0.0 splitter ratio device is speculated to permit and promote the *μVS* intracellular delivery process. It is anticipated that the vortex shedding observed inside the wide wake regions are likely to prolong the flow duration (increase cell residence duration) for the intracellular delivery process to occur. Therefore, it is critical to conduct a set of DOEstudy with different column pitch separations for achieving the optimal performance. This work is currently ongoing.

Instantaneous flow parameters such as vorticity and streamwise velocity are useful to evaluate vortex behaviours in both near-field and far-field regions. Supplemental Figure 2 shows a close up view of a pair of spanwise oscillating vortex structures identified in 0.0 and 0.25 splitter ratio devices. In 0.0 splitter ratio device, the spanwise oscillating vortex pairs are present, starting from each side of the post. Such vortex shedding oscillation behavior extended further downstream to the free wake region. Far-field wake development also occurred in devices with separation ratios >3.2. In all other cases, the near-field vortex shedding was attenuated in near-field and prohibited any further wake development in far-field.

Q-criterion Iso-Surfaces Q-criterion detection technique was used to visualize vortex structures in three-dimensional space. Supplemental Figure 3 demonstrates the 3D vortex structures detected in between columns 1 and 2 (right) and 5 and 6 (left). Large scale vortices were detected between column 5 and 6 for 0.25 and 0.0 splitter ratio devices. Large scale vortices were found to behave in coherence as expected. In contrast, minimal vortex structures were detected upstream between column 1 and 2. These Q-criterion results were consistent with the spanwise vorticity contours previously observed and described above. For 0.25 and 0.0 splitter ratio devices, coherent vortices oscillated at much higher amplitude at downstream columns than in upstream columns.

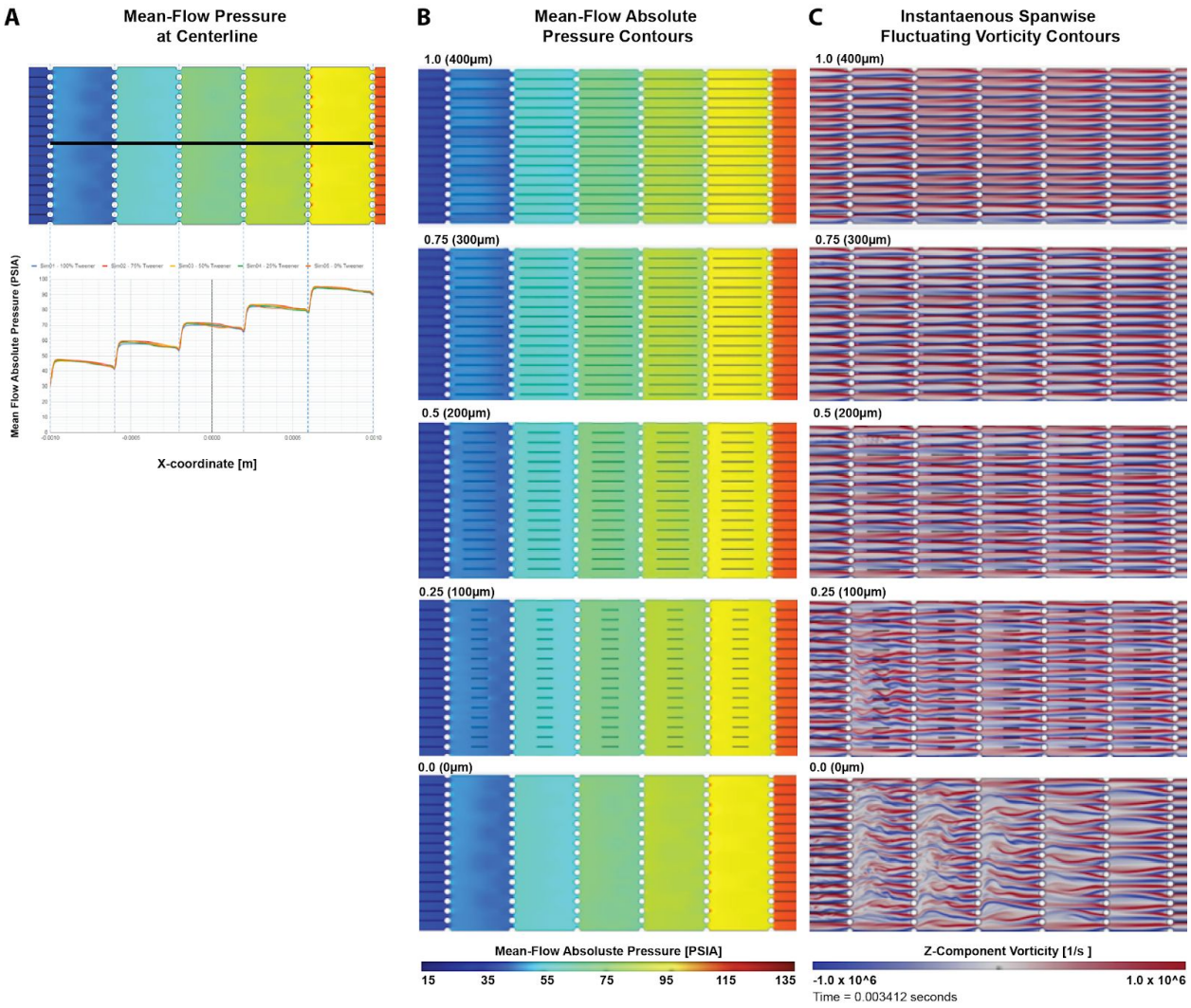

Supplemental Figure 1. Simulated Mean-Flow Hydrodynamic Pressure Distributions and Contours and Instantaneous Spanwise Fluctuating Vorticity Contour of *µVS* devices. (A) Mean-flow hydrodynamics pressure distribution at the centerline of the chip. Distribution is from the 1st to 6th (of 6) post-columns. Hydrodynamic pressure uniformly distributed in spanwise direction (top). Local pressure drops were detected across each post column in the streamwise direction for all design configurations (bottom). (B) Absolute pressure and (C) instantaneous spanwise fluctuating vorticity magnitudes in the flow fields pseudocolored for all *µVS* devices designs.

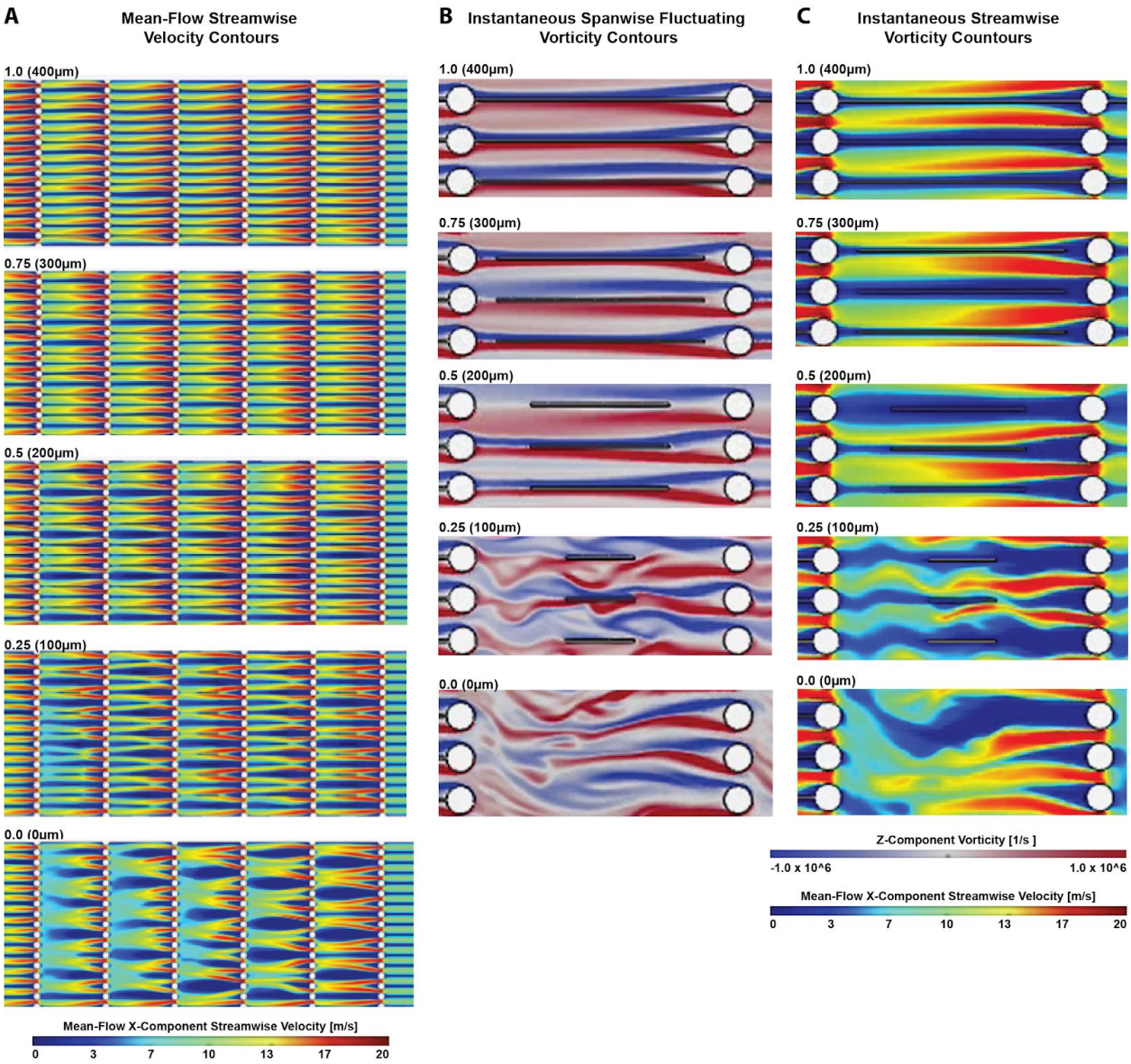

Supplemental Figure 2. Simulated Flow-Field Contours as Mean-Flow Streamwise, Instantaneous Spanwise Fluctuating and Instantaneous Streamwise Velocity Contours of *µVS* devices. Mean-flow streamwise (A) and instantaneous spanwise (B) and instantaneous streamwise vorticity (C) contour distribution for all *µVS* device designs.

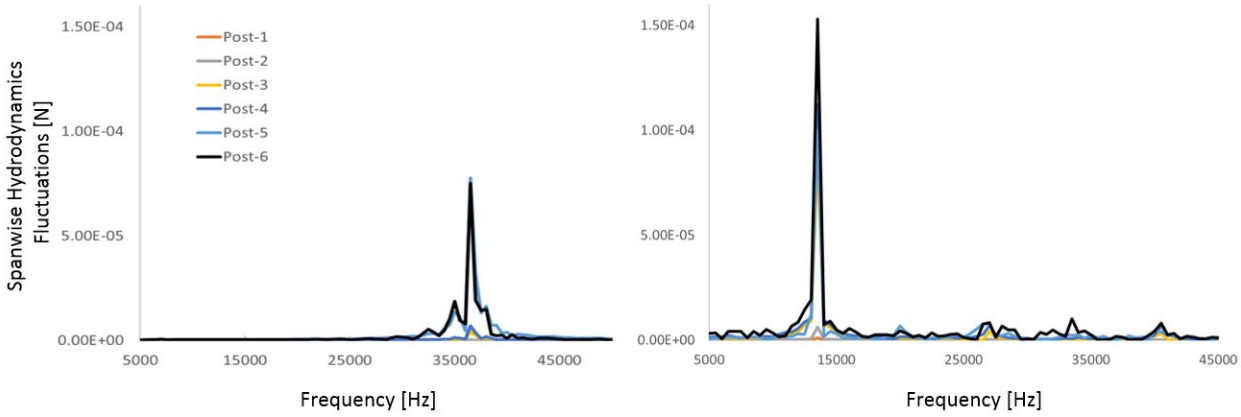

Supplemental Figure 3. Simulated Spanwise Hydrodynamic Forces Spectral Frequency of *μVS* devices. Spanwise hydrodynamics forces spectral amplitude of both SIM04 (left, 0.25 splitter ratio) and SIM05 (right, 0.0 spitter ratio).

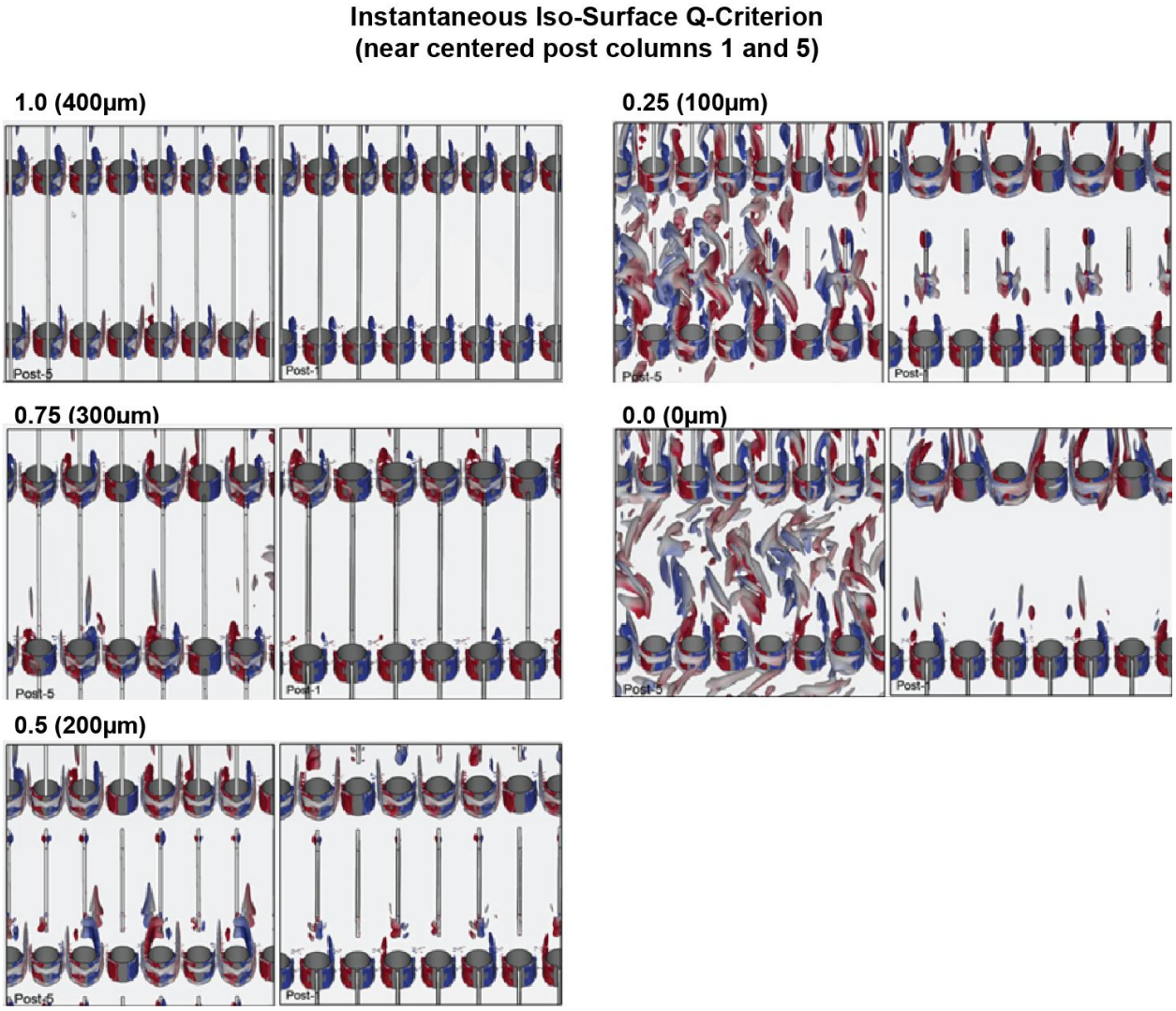

Supplemental Figure 4. Simulated Q-criterion Iso-surfaces to visualize vortex structures in *µVS* devices. Q-criterion in flow-field simulated to visualize structures in three-dimensional space. Simulation images show Q-criterion iso-surface at post-columns 1 (right) and 5 (left) for all *µVS* device designs.

Supplemental Methods. Post Near Wake Indicator (PNWI)

PNWI is defined as Post Near Wake Indicator derived from the hydrodynamics fluctuating forces. The PNWI % calculation is based on the following steps:

1) Time history of total spanwise absolute hydrodynamics forces for each post column is recorded.
2) The standard deviation of total spanwise absolute hydrodynamics forces for each column is computed. This result gives hydrodynamics fluctuations about the mean.
3) Ratio to 0% tweener for each case is computed based on the standard deviation computed from Step 2.
4) This ratio is named “Post Near-Wake Indicator (PNWI)”. The general formula of PNWI is:

$$PNWI\% = \sqrt{\frac{\sum(F_i - F_{mean})^2}{\left[\sum(F_i - F_{mean})^2\right]_{ref}}} \times 100\%$$

where F_i is absolute hydrodynamics forces measured at each post and F_{mean} is averaged (mean) hydrodynamics forces measured at each post.